



Multi-modality measurement and comprehensive analysis of hepatocellular carcinoma using synchrotron-based microscopy and spectroscopy

Gong-Xiang Wei¹ · Sui-Xia Zhang² · Zhao Li¹ · Fu-Li Wang³ · Yan-Ling Xue⁴ · Te Ji⁴ · Hui-Qiang Liu^{1,2}

Received: 12 May 2021 / Revised: 21 June 2021 / Accepted: 24 June 2021 / Published online: 13 September 2021

© China Science Publishing & Media Ltd. (Science Press), Shanghai Institute of Applied Physics, the Chinese Academy of Sciences, Chinese Nuclear Society 2021

Abstract The visualization and data mining of tumor multidimensional information may play a major role in the analysis of the growth, metastasis, and microenvironmental changes of tumors while challenging traditional imaging and data processing techniques. In this study, a general trans-scale and multi-modality measurement method was developed for the quantitative diagnosis of hepatocellular carcinoma (HCC) using a combination of propagation-based phase-contrast computed tomography (PPCT), scanning transmission soft X-ray microscopy (STXM), and Fourier transform infrared micro-spectroscopy (FTIR). Our experimental results reveal the trans-scale micro-morphological HCC pathology and facilitate quantitative data

analysis and comprehensive assessment. These results include some visualization features of PPCT-based tissue microenvironments, STXM-based cellular fine structures, and FTIR-based bio-macromolecular spectral characteristics during HCC tumor differentiation and proliferation. The proposed method provides multidimensional feature data support for constructing a high-accuracy machine learning algorithm based on a gray-level histogram, gray-gradient co-occurrence matrix, gray-level co-occurrence matrix, and back-propagation neural network model. Multi-dimensional information analysis and diagnosis revealed the morphological pathways of HCC pathological evolution and we explored the relationships between HCC-related feature changes in inflammatory microenvironments, cellular metabolism, and the stretching vibration peaks of biomolecules of lipids, proteins, and nucleic acids. Therefore, the proposed methodology has strong potential for the visualization of complex tumors and assessing the risks of tumor differentiation and metastasis.

Gong-Xiang Wei and Sui-Xia Zhang have contributed equally.

This work was supported by the Natural Science Foundation of Shandong Province, China (No. ZR2020MA088), Natural Science Foundation of Xinjiang Uygur Autonomous Region, China (No. 2019D01C188), National Key Research and Development Program of China (No. 2018YFC1200204), and National Natural Science Foundation of China (No. 12175127).

✉ Hui-Qiang Liu
liuhq@sdut.edu.cn

¹ School of Physics and Optoelectronic Engineering, Shandong University of Technology, Zibo 255000, China

² State Key Laboratory of Pathogenesis, Prevention, Treatment of Central Asian High Incidence Diseases, First Affiliated Hospital of Xinjiang Medical University, Urumqi 830054, China

³ Oncology Department, ZiBo Central Hospital, Zibo 255000, China

⁴ SSRF, Shanghai Advanced Research Institute, Chinese Academy of Sciences, Shanghai 201800, China

Keywords Propagation based phase contrast tomography · Soft X-ray microscopy, · Infrared micro spectroscopy · Machine learning · Tumor microenvironment and metastasis

1 Introduction

With the continued development of various technologies, such as microtomography and micro-spectroscopy, biomedical measurement and diagnosis have transitioned from traditional medical imaging to multi-dimensional imaging and information fusion, and conversion has been gradually applied to clinics to perform tumor detection and

treat soft tissue injuries, and cardiovascular and cerebrovascular diseases [1–3]. Many cross-disciplinary studies have been conducted on the in situ micromorphological measurement of tumor complex systems, the topological evolution of angiogenesis networks, cellular inner structural changes, assessment of nanoparticle drug safety, and multi-dimensional data associations over the past decade [4–7]. Most early soft-tumor-related lesions are on the sub-millimeter or micron scale, meaning they are difficult to detect using traditional computed tomography (CT), magnetic resonance imaging, and ultrasound techniques based on their relatively limited sensitivity and resolution. Pathological examinations using electron or optical microscopes can be performed at the micron or sub-micron scale, but they require complicated and time-consuming preprocessing and cannot obtain 3D sectional images. However, the 3D micro-characterization of soft tissue tumor nodules and angiogenesis is essential for studying tumor growth, development, and early diagnosis [8–10]. Furthermore, the detection of organic biomacromolecules is becoming increasingly important for the analysis and discovery of tumor markers, which has significantly promoted the development of fluorescence and infrared (IR) microscopy techniques [11, 12]. One of the most pressing problems facing current cancer research is the establishment of trans-scale and multi-dimensional information correlation analysis from tissues to cells and even biomolecules. This study aimed to measure the multi-modality imaging analysis, data fusion, and pathological diagnosis of hepatocellular carcinoma (HCC) quantitatively. HCC is a heterogeneous tumor associated with chronic infection and cirrhosis caused by metabolic syndrome, alcohol consumption, and viral infection by the hepatitis B/C virus. According to the neoplasm staging, hepatic function, and patient physiological status, HCC therapeutic management mainly includes chemoembolization, transplantation, or resection of the liver. However, the prognosis is unsatisfactory, because the complexity of HCC prevents the major goals of accurate diagnosis, determination of tumor biological boundaries, and therapeutic approaches. The multi-modality measurement and comprehensive analysis of HCC will help us better understand the growth of HCC and provide more specific data for early diagnosis and clinical research on HCC [13–17].

Synchrotron-based high-resolution microscopic and spectral techniques have been established for detecting different modality signals of the interactions of X-rays and biological tissues. These techniques benefit its high-brightness, and a broad and continuously adjustable spectral range. The structural and spectral information of weakly absorbing samples with a high signal-to-noise ratios (SNRs) can be obtained using different imaging techniques and demodulation algorithms [18–21]. There

have been many studies on tumor-related micro-pathomorphology using hard X-ray propagation-based phase-contrast tomography (PPCT) over the past few decades. Micro-pathomorphology is involved in soft tissue tumorigenesis, the tumor neovascularization network, injury of the spine, hepatic echinococcosis, liver cirrhosis and fibrosis, and pulmonary emphysema [22–26]. Fine non-destructive 3D structural features at the micron level can be visualized and analyzed quantitatively, thereby promoting early diagnosis and treatment. For the investigation of nanoparticle medicine and morphological characteristics at the nanoscale, soft X-ray scanning transmission microscopy (STXM) has been developed to probe changes in cell morphology and the intracellular distribution of nanoparticles [27, 28]. The Fourier transform IR spectroscopy (FTIR) technique has been employed for tumor-related mechanism analysis and the discovery of bio-macromolecular markers [29, 30]. It has the advantages of multiple forms of testing samples, such as soft tissues, cells, hair, saliva, blood, and urine. In particular, the non-destructive FTIR technique with synchrotron radiation (SR) is well developed for biomacromolecule detection and is characterized by a higher SNR and label-free analysis of cellular functionality. A typical SR-FTIR spectrum of a biological specimen can reveal the vibrational signals of different organic macromolecules and their functional groups based on the following characteristic spectral regions: (1) nucleic acid fingerprint region of $750\text{--}1400\text{ cm}^{-1}$, (2) protein region of $1450\text{--}1750\text{ cm}^{-1}$; and (3) the lipid region of $2750\text{--}3150\text{ cm}^{-1}$, which are closely associated with the structural changes of different molecular compositions. Therefore, the SR-FTIR method plays an important role in analyzing biomacromolecules and dynamics in the single-cell dimension. In this study, we developed an integrated solution combining imaging and spectroscopy, including PPCT, STXM, and SR-FTIR [31, 32]. HCC samples were used for multi-modality experiments with simple sample preparations. A PPCT dataset and quantitative analysis were jointly used to reveal 3D tissue microstructural features, microcirculatory network changes, and the relationships between tumor morphological development and the microenvironment without requiring specimen sectioning. STXM data can provide images of an entire HCC cell without staining at a resolution of 30 nm, and small-tissue and cellular changes can be distinguished and classified automatically using a machine learning algorithm. In this study, we employed the back-propagation neural network (BP-NN) algorithm based on its capabilities for image feature extraction from gray-level histograms (GHs), gray-gradient co-occurrence matrices (GGCMs), and gray-level co-occurrence matrices (GLCMs) [33–35]. Staining cells or tissues with exogenous labeling tags often leads to poor specificity based on cross-

reactions of biomacromolecules. Non-staining SR-FTIR is able to obtain HCC subcellular structural fingerprints and organic composition distributions. Therefore, the proposed trans-scale and multi-modality data acquisition and analysis method will be helpful for developing HCC tumor evaluation criteria with multi-quantitative parameters, including tumor inflammatory environment, angiogenesis, cell morphology, and biomacromolecule spectroscopic features.

2 Materials and methods

2.1 Tissue and cell samples of liver tumors in vitro

One hundred surgical resection specimens of HCC were provided by the First Affiliated Hospital of Xinjiang Medical University (XJMU) with approval from the ethics committee of XJMU. The inclusion and exclusion criteria for the experimental samples are listed in Table 1.

Histopathological examinations of the HCC tissue (HCCT) specimens revealed moderate or low differentiation in this study. The HCC cell samples were immediately extracted from small postoperative tissue blocks, digested with 0.25% trypsin for 20 min, washed, and then cultured in Dulbecco's modified Eagle's medium (DMEM). The DMEM was modified to contain 4500 mg/L of glucose, 4 mM of L-glutamine, 1 mM of sodium pyruvate, and 1500 mg/L of sodium bicarbonate. It was also supplemented with 10% calf serum, 100 U/mL penicillin, and 100 µg/mL streptomycin for 70–80% confluency on the bottom of the petri dish. The cells were maintained in a 5% CO₂ incubator at 37 °C throughout the experimental process. All experimental samples were divided into two groups of tumor lesion areas and para-carcinoma areas. Prior to the experiments using SR-PPCT, all formalin-fixed tissue samples were processed with a graded dehydration series of ethanol solutions (GDES) and firmly packed in a centrifuge tube to avoid artifacts caused by tiny deformations or movements. For the SR-FTIR experiments, serial tissue sections with thicknesses of 10 µm were obtained using frozen section methods, carefully attached to a BaF₂ substrate, examined under a microscope, wrapped in foil, and stored at – 80 °C to preserve the biochemical

substances in the samples. For SR-STXM measurements, the cellular samples were fixed and dehydrated using GDES at ambient temperature and then dropped onto a Si₃N₄ window for cellular fine structural measurements. Tissue specimens were used for histopathological examination.

2.2 Experimental setup and data processing

A high-brightness light source can facilitate measurements with a high SNR. Our synchrotron-based experiments were conducted on the hard X-ray imaging, soft X-ray microscopy, and IR spectroscopy beamlines at Shanghai Synchrotron Radiation Facility (SSRF). We present a general technique flowchart for combining the SR-PPCT, SR-STXM, and SR-FTIR methods to investigate the pathological mechanisms of biomedical soft tissues via trans-scale-modality correlation analysis in Fig. 1. The 3D morphological tissue changes were observed using SR-PPCT on BL13W1, which is equipped with a complementary metal–oxide–semiconductor with a resolution of 6.5 µm/pixel and different camera lenses (× 1.25, × 2, × 10) for achieving different microtomographic spatial resolutions. All SR-PPCT projections were preprocessed using background correction and phase retrieval to improve the contrast-to-noise ratio and the density resolution of weakly absorbing samples without the use of a contrast agent. The phase-attenuation-duality algorithm was implemented to retrieve a phase map φ_θ at any single projection angle θ using the following formula:

$$\varphi_\theta(\vec{r}) = \frac{\lambda r_e}{\sigma_{KN}} \cdot \ln \left\{ \left[\cos \left(\frac{\lambda R_2}{4\pi M} \nabla^2 \right) - \left(\frac{2\lambda r_e}{\sigma_{KN}} - \frac{\lambda R_2}{4\pi M} \nabla^2 \right) \cdot \sin \left(\frac{\lambda R_2}{4\pi M} \nabla^2 \right) \right]^{-1} \cdot \left(\frac{M^2 I_\theta(\vec{r}_D)}{I_{IN}} \right) \right\},$$

where I_θ is a single projection image, λ is the X-ray wavelength, r_e is the classic atomic radius, and σ_{KN} is the Klein–Nishina total cross section for X-ray photon Compton scattering from a single free electron. $M = (R_1 + R_2)/R_1$, where R_1 and R_2 are the source-to-object and object-to-detector distances, respectively. This method is used for the discrimination of 3D tissue micromorphological variations and visualization of abnormal microcirculation networks, and aids in the collection of high-precision

Table 1 Inclusion/exclusion criteria for HCC specimens in our experiments

| Inclusion criteria | Age | Gender | Race | Tumor staging | Image screening |
|--------------------|---------------------|----------|-----------------------------|------------------------------|-------------------|
| | 20–70 | No limit | No limit | Moderate/low differentiation | Hepatic carcinoma |
| Exclusion criteria | Partial hepatectomy | | Congenital incomplete liver | | Liver defect |

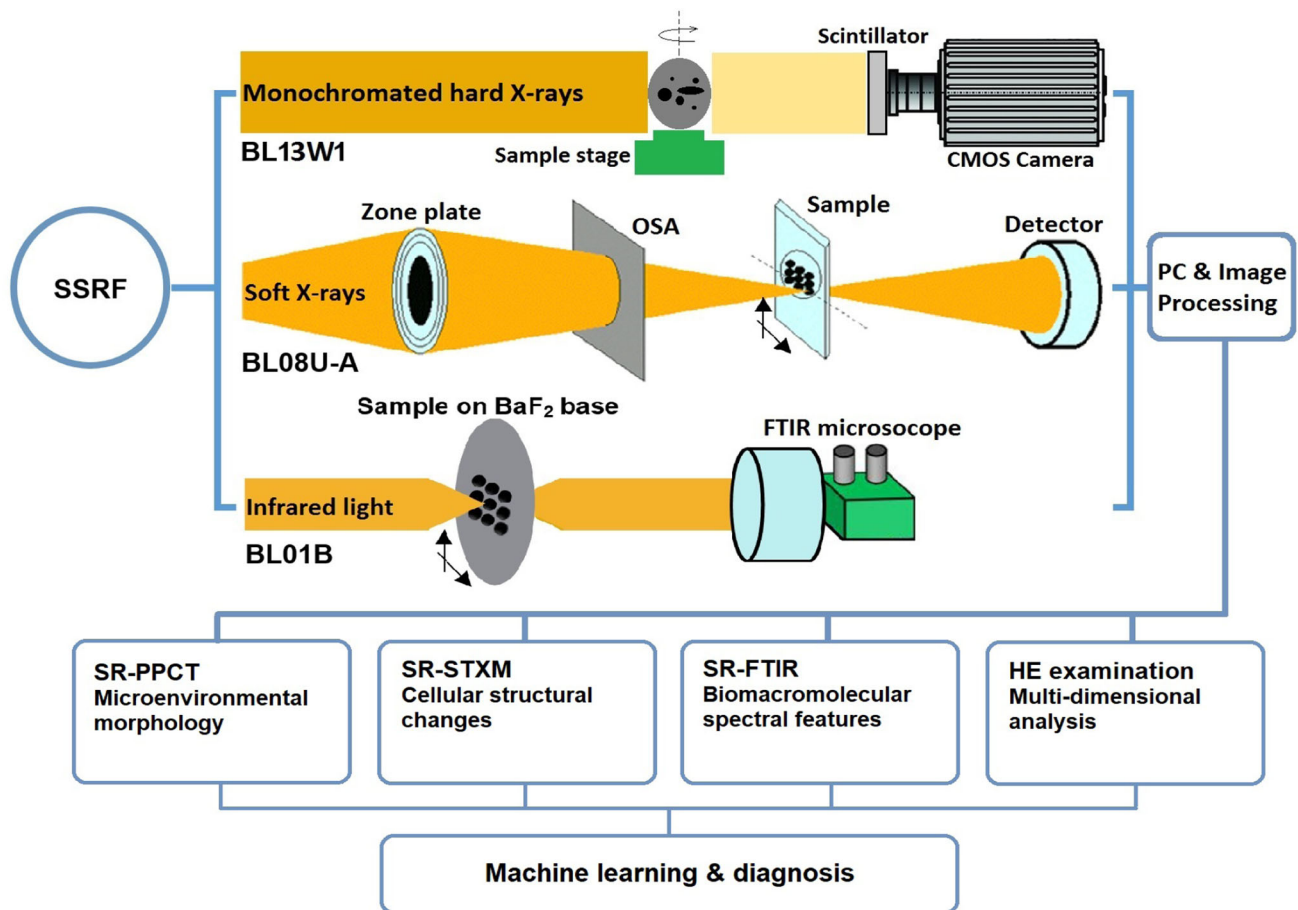


Fig. 1 (Color online) Experimental setups for synchrotron-based PPCT, STXM, and FTIR at SSRF and general technique flowchart for the trans-scale and multi-modality imaging and data analysis of HCC tumors

nondestructive statistics for tissue microenvironmental geometric parameters [36, 37].

The fine feature structures of tumor cells were measured using STXM with a spatial resolution of approximately 30 nm on BL08U1-A. A high-flux soft X-ray beam focused through the zone plate can be used to probe cellular structural information based on the absorption scanning mode [38, 39].

Typical spectra of frozen tumor tissue sections at a spectral resolution of 4 cm^{-1} can be collected using FTIR on BL01B, which is equipped with a Nicolet 6700 FTIR spectrometer and Nicolet Continuum Microscope. In our experiments, a $20\text{ }\mu\text{m} \times 20\text{ }\mu\text{m}$ aperture with a $10\text{ }\mu\text{m}$ step size was applied to acquire mapping data in the wavenumber range of $800\text{--}4000\text{ cm}^{-1}$. In our SR-FTIR experiments, to improve the SNR, the step size was set smaller than the aperture size to produce pixel map overlaps and all data acquisitions were performed three times. The raw mapping spectra were preprocessed with nine-point smoothing and baseline correction to suppress the

ambient noise, electronic offset, dark current, and readout noise of the IR detector further using OMIC 9.0.

3 Results

3.1 SR-PPCT measurement of HCC microenvironments

The rapid proliferation and metastasis of tumors are closely associated with changes in tumor microenvironments. Compared to conventional CT, 3D trans-scale visualizations of HCC soft tissues based on SR-PPCT measurements reveal more detailed pathologic morphological characteristics and microenvironmental changes, as shown in Fig. 2. Macro-moderate or high-differentiation tumor lesions appear as abnormal gray spots or image shadows in Fig. 2(a, b). By using the SR-PPCT technique without staining, HCC-related pathological features can be effectively displayed and distinguished from para-carcinoma liver tissues (PCLT) on the micron scale, as indicated

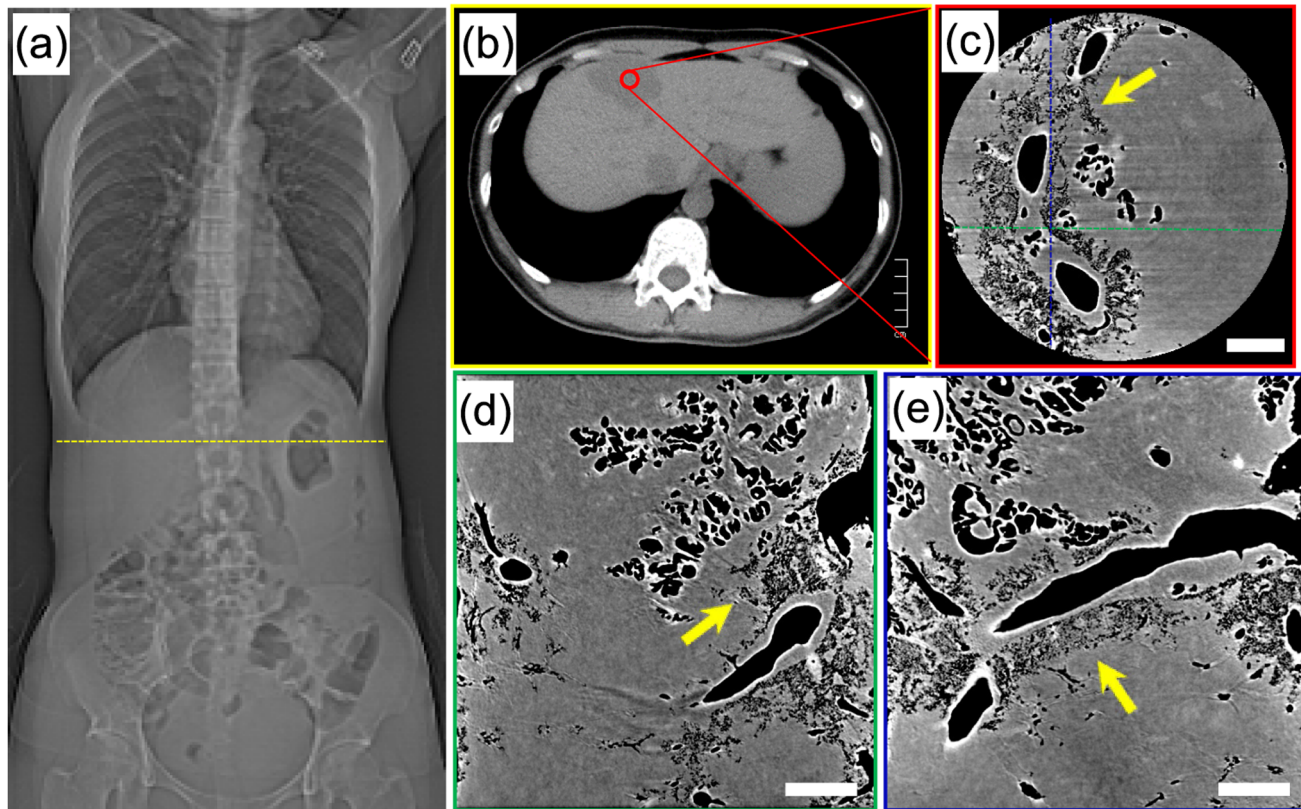


Fig. 2 (Color online) Results of medical imaging and SR-PPCT microtomography of HCC tumors. **a** Radiological image, **b** cross section of traditional CT at the position of the dashed line in **a**, **c** transverse section located in the red circle in **b**, **d** coronal section

located at the position of the green dashed line in **c**, and **e** sagittal section located at the position of blue dashed line in **c** as reconstructed by SR-PPCT. Scale bar in **b** is $10^4 \mu\text{m}$ and scale bars in **c–e** are $100 \mu\text{m}$

by the yellow arrows in Fig. 2c–e. These results can reveal the morphological distributions of arterioles, venules, sacs, internal septa, fibrosis, microcalcification, and increasing inflammation reactions in HCCT from any perspective. Nondestructive 3D inner-structural information regarding PPCT reveals detailed changes in tumor tissues associated with tumorigenesis and metastasis, which are helpful for precise tumor diagnosis.

Angiogenesis and microcirculation network formation play important roles in tumor diagnosis and morphological understanding. We present 3D visualizations of microvascular distributions of HCC solid tumors using different scales and modalities in Fig. 3. The entire HCC vascular network based on conventional CT is presented in (a) and the formation and development of tumors associated with inflammation and micro-cyst clusters near blood vessels based on SR-PPCT are presented in (b, c). The inflammatory microenvironment and blood supply system can trigger the concentration of endothelial and epithelial cells to form micro-cystic clusters, which consist of irregular tumor micro-vessel networks. Based on visual inspections, the blood vessels in normal tissue areas are thicker and have higher curvature. In contrast, the blood vessels of

HCC are relatively thin and stiff, and their distribution is more dispersive and glomerate. According to the comparisons of the high-resolution PPCT and pathologic examination slices in (d, e), SR-PPCT provides more abundant and detailed vascular 3D structures without staining and sample deformation, and reveals the sedimentation of calcium salts with high gray value areas in (d) around the microcysts indicated by yellow arrows. These salts are a concomitant precursor of hepatic fibrosis.

3.2 Joint measurements with high-resolution SR-PPCT and SR-FTIR mapping

The morphological characteristics of hepatic sinusoids were observed using SR-PPCT. The inflammatory microenvironment and formation of sinusoid capillaries in HCC tumors can be clearly visualized based on the high phase contrast and spatial resolution, as indicated by the blue arrows in Fig. 4a–c. These factors promote the formation of abundant irregular micro-vessels around and inside HCC tumors, as indicated by the red arrows in (b) and (c). Furthermore, representative spectra and 2D distributions of biological macromolecules were collected

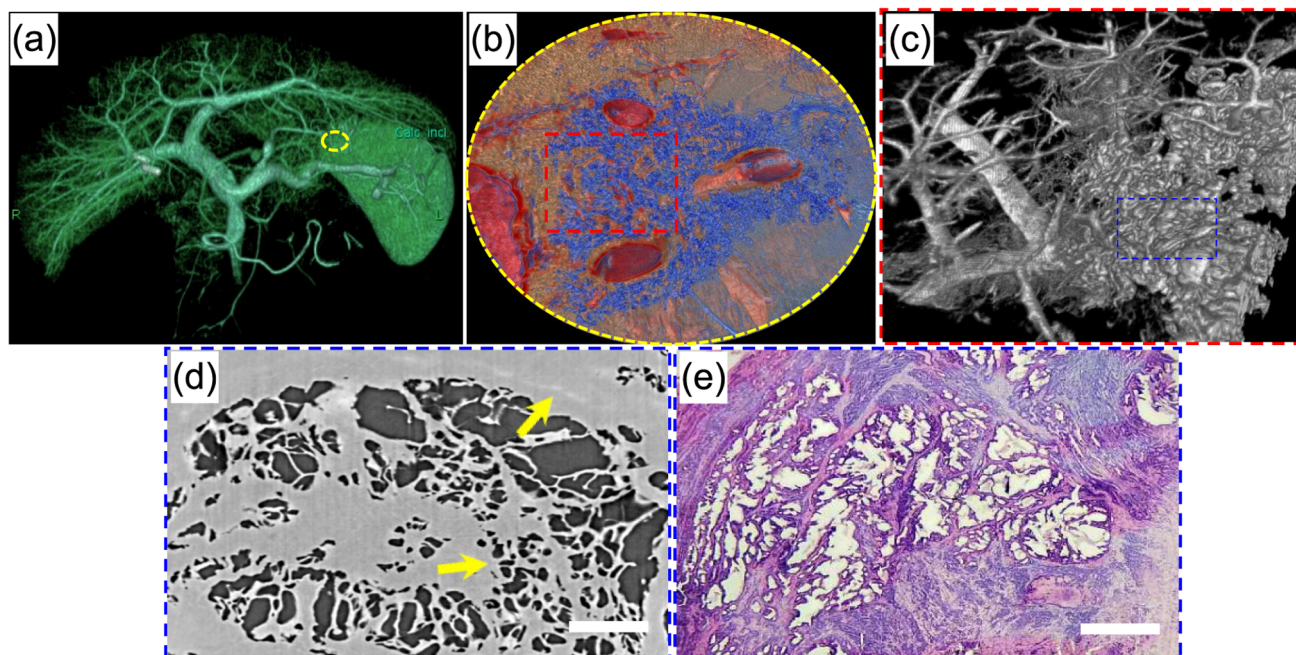


Fig. 3 (Color online) 3D microenvironment of an HCC liver tumor and medical examination comparisons. **a** 3D image of the entire liver and the solid HCC tumor from medical CT, **b**, **c** enlarged reconstructed results based on the PPCT, respectively, located in the yellow

circle area in **a** and red rectangle area in **b**, and **d** PPCT slice and **e** HE slice of the HCC tumor micro-cyst area indicated by the blue rectangle in **c**. One can observe similar HCC tumor lesions between different imaging modalities. Scale bar = 100 μm

via SR-FTIR measurements for association analysis [40, 41]. FTIR mapping measurements with $200\ \mu\text{m} \times 160\ \mu\text{m}$ areas were performed in both the PCLT and HCCT regions, which are denoted by the red and orange rectangles, respectively, in (a). Images (d) and (h) were captured in FTIR microscopic images for the selection of PCLT and HCCT tissue regions of interest (ROIs) based on the SR-PPCT results and pathologist analysis. The measurements of each sample were repeated three times on average. Twenty samples were randomly selected for each group and three groups were selected. Chemical distributions and concentration maps were processed using normalized pseudo-color scale bars to identify lipids, proteins, and nucleic acids, which correspond to peaks at 2922, 1649, and $1074\ \text{cm}^{-1}$, respectively, as shown in parts (e, f, g, i, k, l). One can clearly see that the concentrations of the nucleic acid and lipid components in the HCCT areas increase significantly.

3.3 SR-STXM measurement of HCC cellular structures

The SR-STXM technique was also employed to measure the HCC cellular structures of liver cells, endothelial cells of the blood sinus, and Kupffer cells, as shown in Fig. 5a–f. One can see that the HCC-related nucleoli are divided and diffused to varying degrees, as indicated by the white arrows in (b, e, f). A large amount of cellular secretions and

lipid droplets emerge chaotically, as indicated by the blue arrows in (c, d, e). Compared to (a), the mitochondria and cytoplasmic volume in HCC cells increases significantly, as indicated by the red arrows in (c, f). A more detailed cellular structure of HCC-related changes can be observed without staining by using high-resolution SR-STXM measurements, as shown in (f). The large aggregation of mitochondria, endoplasmic reticulum, and glycogen is associated with the fast metabolism of HCC cells and active tumor microcirculation. Additionally, nucleosome dispersion and cell membrane morphological changes are helpful for understanding the occurrence, metastasis, and staging of HCC.

3.4 SR-FTIR measurement of HCC biomacromolecules

The biomolecular vibration absorption peaks and characteristic IR spectral regions were successfully measured and are presented in Fig. 6a, b, corresponding to the PCLT and HCCT functional group vibrations. The spectral range of $3500\text{--}3100\ \text{cm}^{-1}$ is attributed to O–H & N–H bond stretching vibrations in the cellulose and polyamide, and the range of $3050\text{--}2800\ \text{cm}^{-1}$ is attributed to the symmetric and antisymmetric stretching vibrations of methyl and methylene C–H bonds, which are related to the increasing lipid-related acyl chains of HCCT. The peaks at 1649 and $1485\ \text{cm}^{-1}$ are attributed to the protein amide I

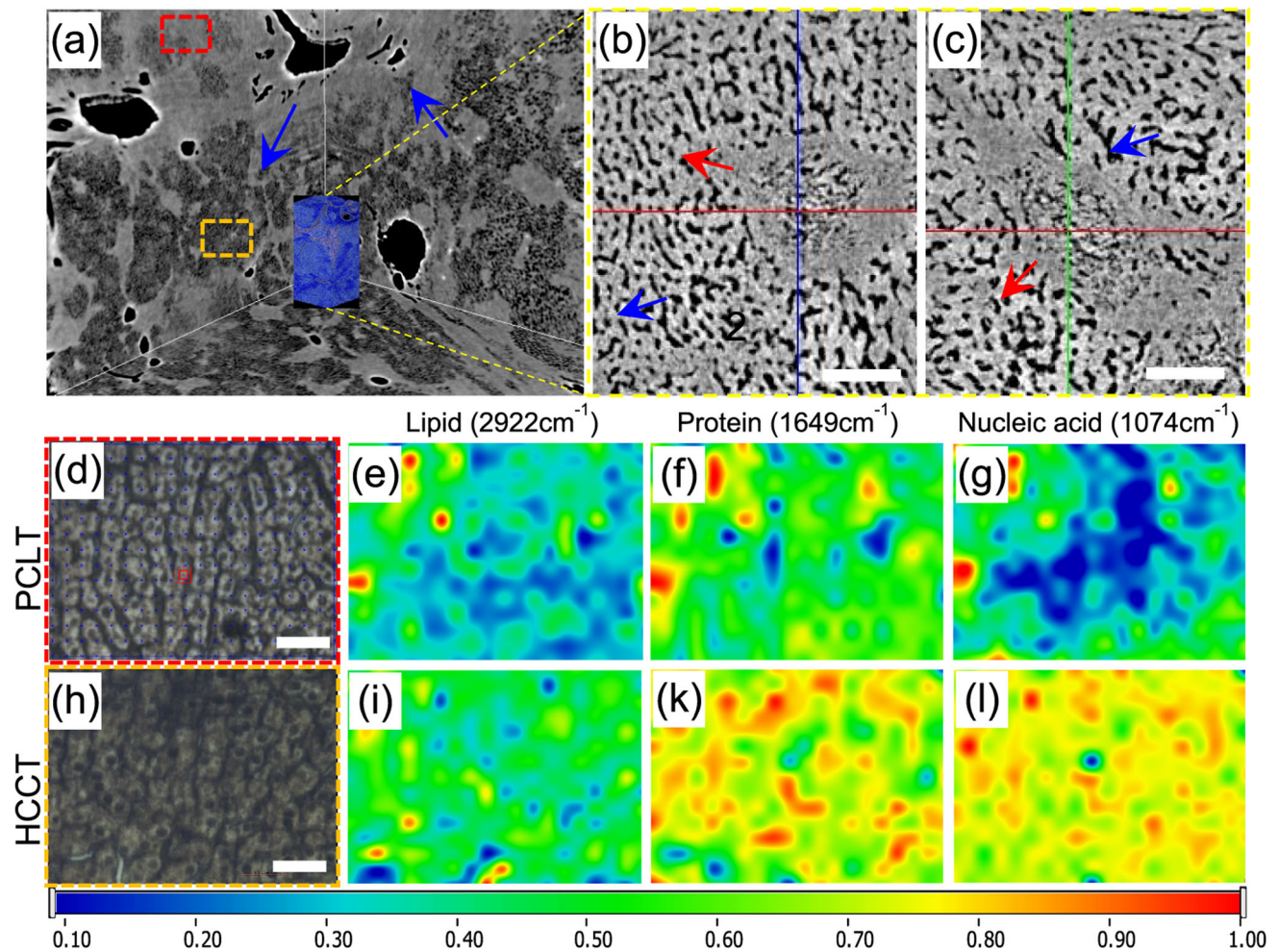


Fig. 4 (Color online) Microstructural and organic macromolecular feature spatial distributions in HCCT based on SR-PPCT coupled with $10\times$ objective lens and SR-FTIR techniques. **a** 3D microenvironment of HCC and its virtual tumor block, **b**, **c** fine structural distribution of hepatic sinusoids (blue arrows) and the formation of sinusoid capillaries (red arrows) in different sections of **a**, **d**, **h** optical microscopic images of PCLT and HCCT tissue layers indicated by the

red rectangle in **b** and orange rectangle in **c**. Univariate maps for collecting the chemical spatial distributions of lipids, proteins, and nucleic acids in the layers of PCLT and HCCT regions in different feature infrared spectra. **e**, **i** Lipids recorded with a feature peak at approximately 2922 cm^{-1} . **f**, **k** Distributions of proteins with a feature peak at approximately 1649 cm^{-1} . **g**, **l** Distributions of DNA at 1074 cm^{-1} . Scale bars: $50\text{ }\mu\text{m}$ in **b**, **c** and $30\text{ }\mu\text{m}$ in **d**, **h**

(N–H bending and C=O stretching) and protein amide II (C–N stretching and N–H bending), reflecting changes in nucleolus histones. In the chemical distribution image, one can see that the content of protein amide increases in HCCT. The spectra at 1453 and 1397 cm^{-1} are attributed to C–H bending vibrations and COO– symmetric stretching vibrations, respectively. The range of 1209 – 1074 cm^{-1} represents the symmetric and antisymmetric stretching vibrations of nucleic acids consisting of phosphorylated molecules (PO_2 phosphodiester stretch) and glycogen, respectively. In comparison, there is a significant increase in the concentration of nuclear acids between 1000 and 1300 cm^{-1} , which is associated with DNA phosphorylated carbonated nucleoli. The spectral band of 900 – 1000 cm^{-1}

for HCCT appears more active, which is related to RNA ribose chains.

4 Analysis and discussion

For quantitative analyses of HCC microenvironmental changes, ROIs were selected from the areas of PCLT, outside areas of HCCT (HCCT_{out}), and inside areas of HCCT (HCCT_{in}) in 20 postoperative specimens, which were randomly selected from 100 experimental specimens and defined by our surgeon and pathologist. There were 60 ROIs in total (20 ROIs for each area), $150\text{ }\mu\text{m} \times 150\text{ }\mu\text{m}$ voxels for each ROI, $6.5\text{ }\mu\text{m}^3$ per voxel, and a volume of 0.975 mm^3 per ROI. We defined the 3D micro-

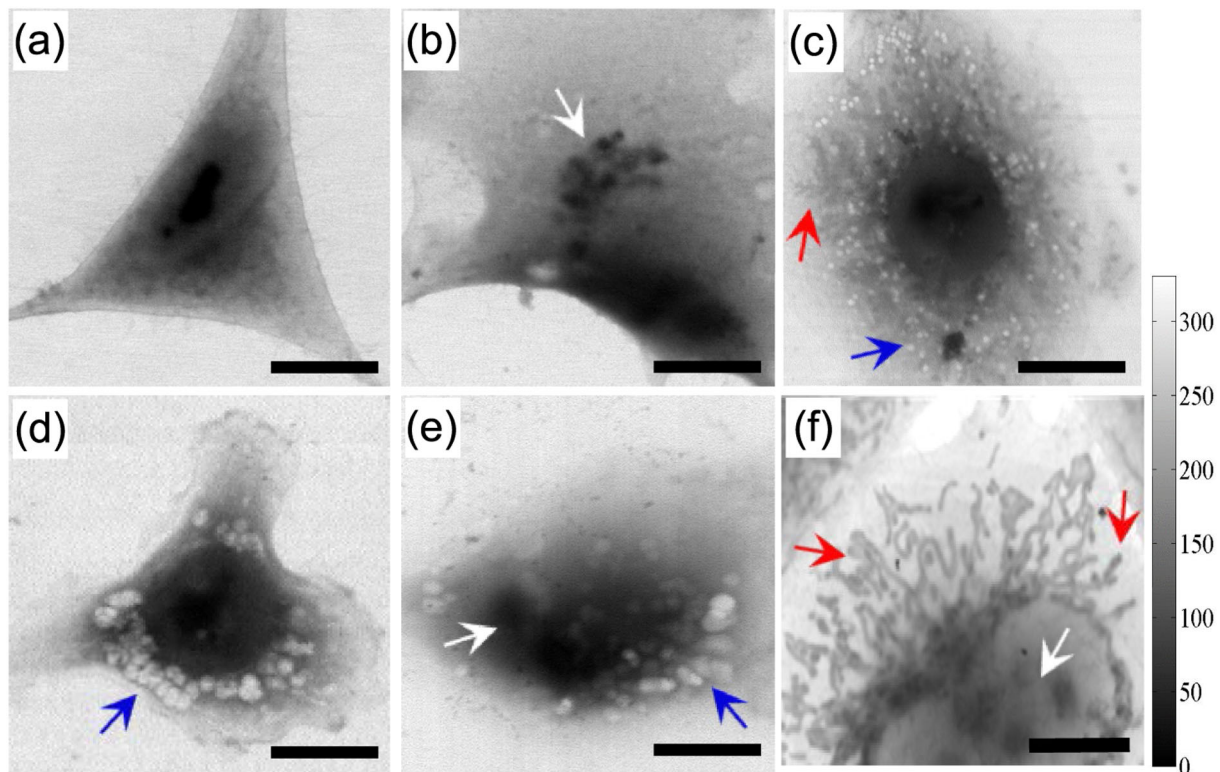


Fig. 5 (Color online) Features of HCC cells reconstructed by and SR-STXM techniques. Images of different hepatocytes obtained from SR-STXM: **a** stellate hepatocyte, **b** Kupffer's cell, **c** liver plate cell, **d** endothelial cell of blood sinus, **e** epithelial cell of connective tissue,

f enlarged Kupffer's cell with mass of mitochondria. Blue arrows denote lipid globules or exosomes of hepatocytes, red arrows denote mitochondria, and white arrows denote nucleoli. Scale bars: 50 μm in **a**, **e**, 10 μm in **b-d**, **f**, **g**, and 5 μm in **h**

vessel density (3D-MVD) as follows: $3\text{D-MVD} = (\text{voxels of micro-vessels})/(\text{total voxels in RoI})$. Statistical results for the microvascular numbers, microcyst numbers, and inflammation areas are presented in Fig. 7. The t test statistical method was employed to compare the datasets with a normal distribution and p value threshold of 0.05 representing statistical significance. This demonstrated that the SR-PPCT technique combined with phase retrieval enables the visualization of the boundaries of tumors and normal tissues, as well as the microvascular networks in tumor infiltration regions. We found that the smallest sinusoid capillaries abundantly scattered along the edges of HCC tumors are approximately 10 μm in diameter, which is a possible early diagnosis feature of HCC. This indicates that HCC is a typical multi-vascular solid tumor and that an inflammatory microcystic environment is the basis of tumor angiogenesis, which is characterized by uncontrolled growth and metastasis.

This analysis is useful for the intelligent diagnosis and feature delineation of different differentiated tumors and for classifying the tumor microenvironmental changes by using machine learning based on SR-PPCT sectional images. There are 10 types of eigenvalues defined by GLCM, GGCM, and GH [42, 43], as shown in Table 2. The

eigenvalue datasets were calculated in three groups (PCLT, HCCT_out, HCCT_in, 100 samples per set, 300 samples total). Then, a BP-NN model with 10 hidden layers was employed to classify the three HCC tumor microenvironments with different degrees of differentiation, as shown in Table 2. The calculation of hidden layers (H) is $H = (E + G)^{1/2} + a$, where E is the number of image eigenvalues (input layer), G is the group number for classification (output layer), and a is a constant ranging from 1 to 10 for estimating the number of hidden neurons. For training the BP-NN model, 70%, 15%, and 15% of the samples were randomly selected as training, testing, and verification samples, respectively. The optimal iteration times (I), network performance, gradients, and R values of linear regression fitting degrees were used to evaluate the neural models with different number of hidden layers (H). When $H = 10$ and $I = 19$, the R values for the training, validation, testing, and all samples were all above 0.90.

Based on the differences between the upper and lower quartiles of each sample eigenvalue, the distributions of tumor microenvironment morphologies in all sample spaces are plotted in Fig. 8a, which quantitatively represents the HCC-induced micro-morphological variations between the control group (PCLT), benign group

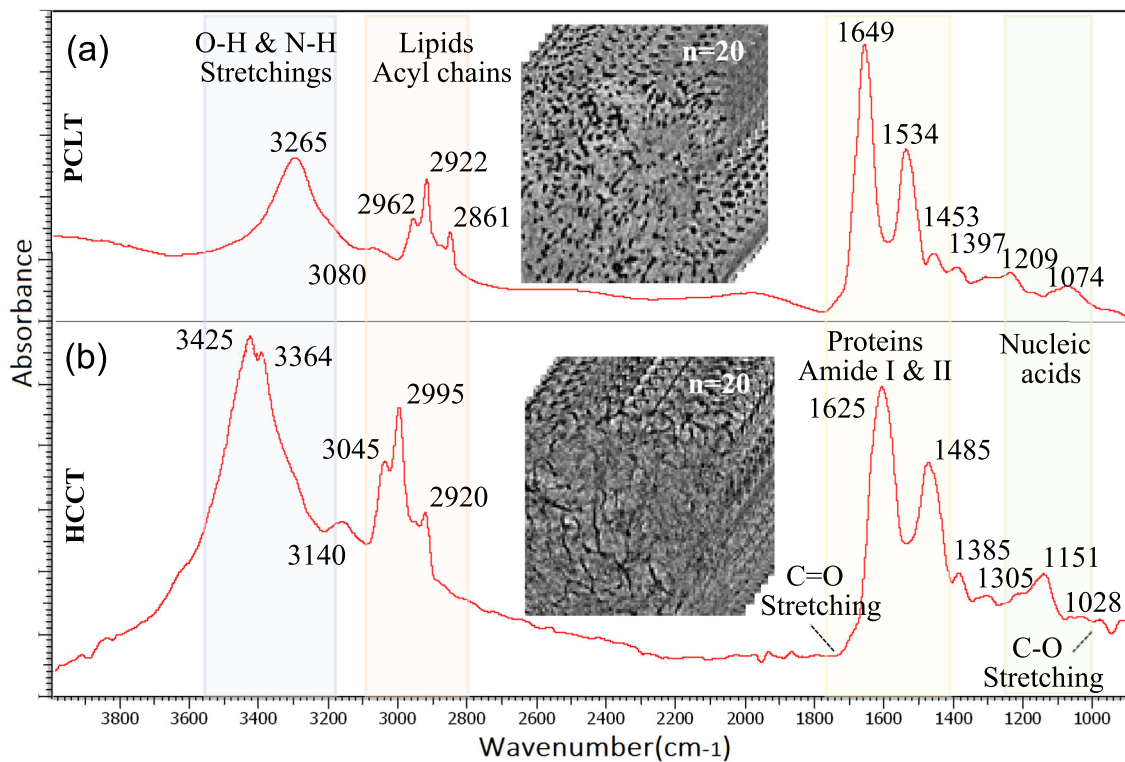


Fig. 6 (Color online) IR spectroscopic results for PCLT and HCCT layers collected in the transmission mode of SR-FTIR. The vibrational absorptions of the most important biomolecules are highlighted in **a** and **b** based on the averages of $n = 20$ randomly selected data from the PCLT and HCCT samples, respectively

Fig. 7 (Color online) Analysis of pathological variations of different HCCT groups. **a** 3D-MVDs and **b** microvascular numbers of PCLT and HCCT, respectively. **c** Inflammation areas and **d** microcyst numbers on the outside surface and inside of HCCT, which affect the development degree of HCC tumor infiltration and its cell proliferation

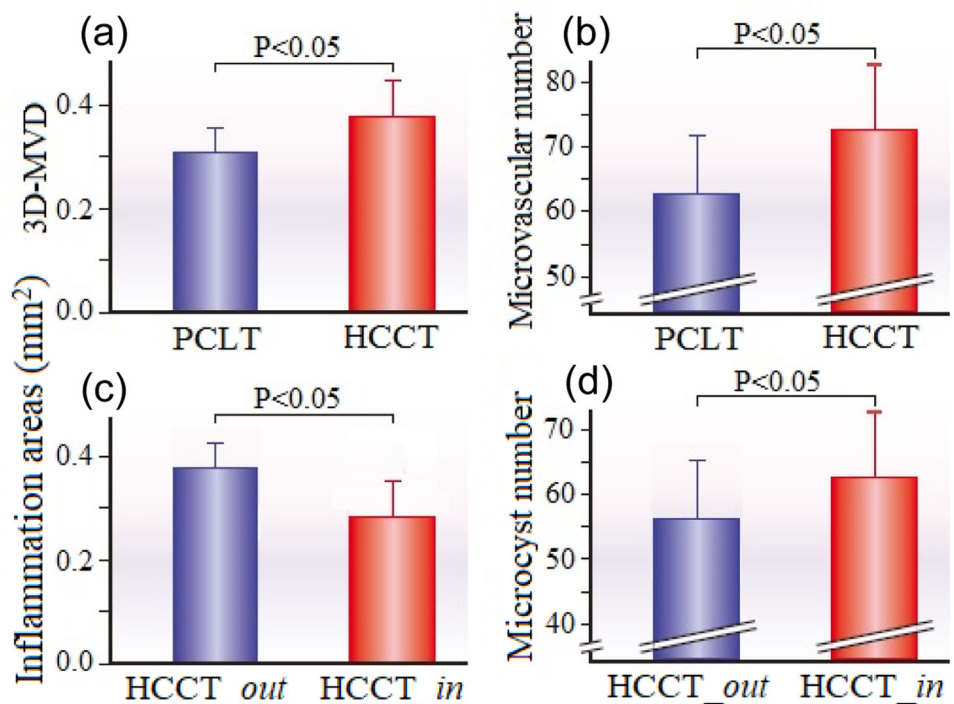


Table 2 Eigenvalue construction for HCC tumor micro-morphology

| Feature types | Grayscale and texture characteristics | | | | | |
|---------------|---|----------------------|----------------------|--------------------|-------------|----------|
| Eigenvalues | Mean value ($E1$), Variance ($E2$), Skewness ($E3$), Kurtosis ($E4$), Energy ($E5$), Homogeneity ($E6$), Contrast ($E7$), Correlation ($E8$), Gray entropy ($E9$), Gradient entropy ($E10$) | | | | | |
| BP-NN model | | | | | | |
| | Input layer (E) | Output layer (G) | Hidden layer (H) | Iterations (I) | Performance | Gradient |
| Preferences | 10 | 3 | 10 | 19 | 0.199 | 0.114 |

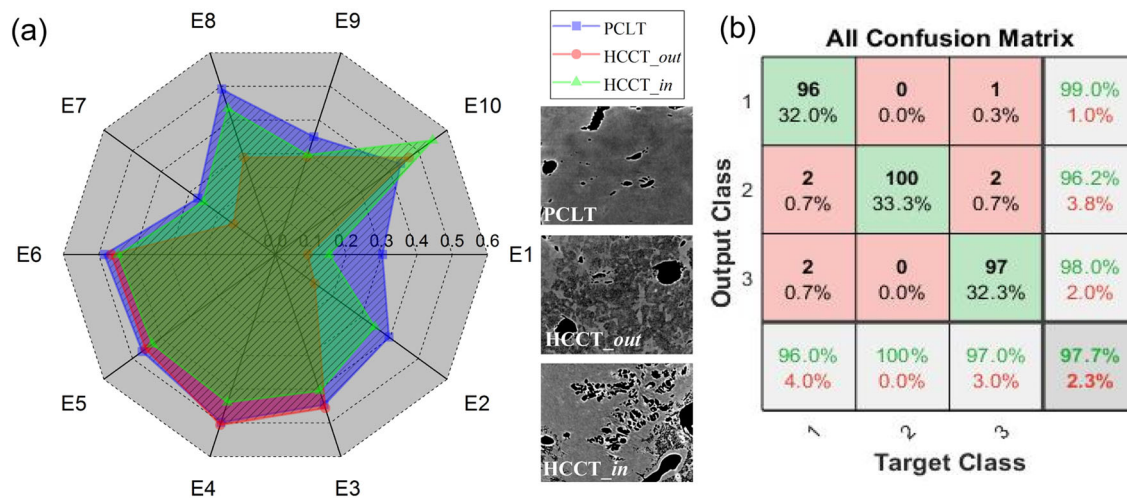


Fig. 8 (Color online) Image feature distributions of HCCT microenvironmental variations and classification results based on the BP-NN model. **a** Maps of 10 image eigenvalues in three groups, and **b** the

confusion matrix of the BP-NN model, which represents the accuracies of three output classes

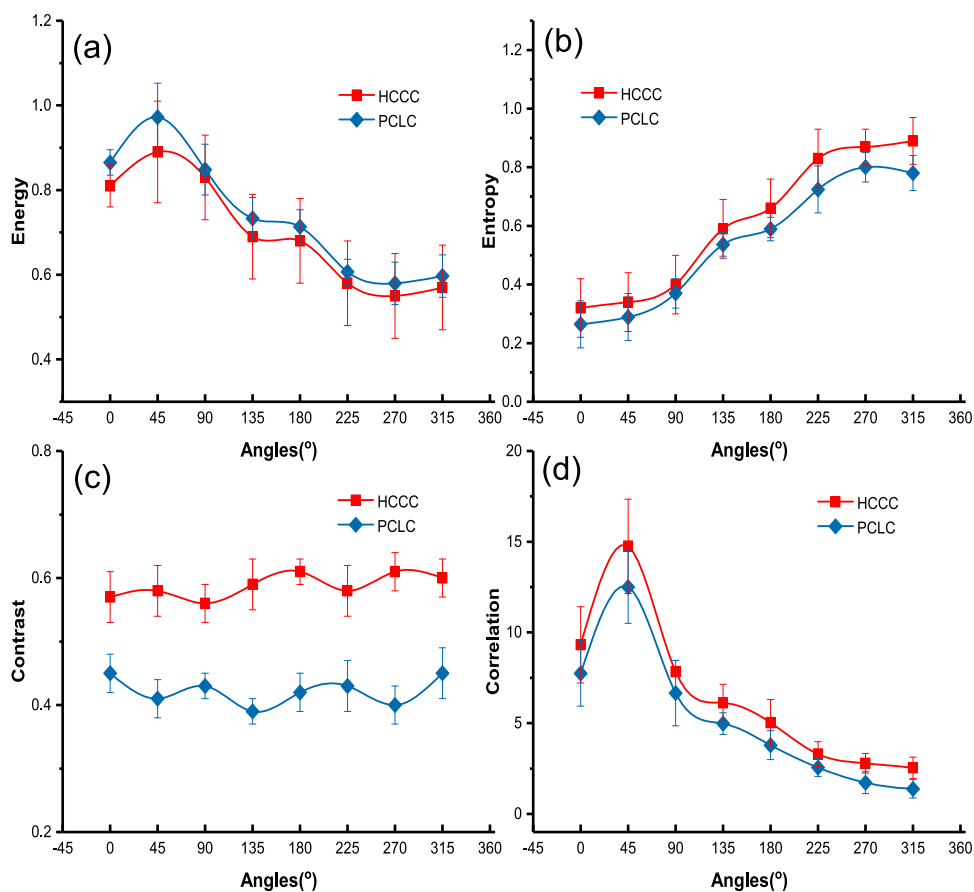
(HCCT_out), and malignant group (HCCT_in). The BP-NN model was employed to classify the three types of HCC microenvironmental morphologies, as shown in Fig. 8b. The accuracy of the BP-NN model is as follows: 96.0% for type_1 (PCLT), 100% for type_2 (HCCT_out), 97.0% for type_3 (HCCT_in), and 97.7% for all samples. To evaluate classification accuracy, the precision and recall rates were calculated as 0.980 and 0.990, respectively. Therefore, the BP-NN model has the potential to classify and diagnose HCC micro-scale tissue variations based on an SR-PPCT database, which is helpful for the quantitative analysis of the pathological correlations between micro-environment changes and tumor development.

Based on the experimental results presented in Fig. 5, HCC-induced cytopathic effects were measured using SR-STXM. The GGCM-based eigenvalues of cellular images were employed to evaluate cellular morphological changes intelligently by calculating the grayscale and texture characteristics of SR-STXM images. Eight rotation angles were considered for each image (0° , 45° , 90° , 135° , 180° , 225° , 270° , and 315°) to calculate four different

characteristics, as shown in Fig. 9. These results effectively reveal the inner microstructural differences between the peri-carcinomatous liver cells (PCLC) and hepatocellular carcinoma cells (HCCC). Compared to the characteristic values of PCLC, the energy of HCCC is lower overall and the entropy, contrast, and correlation of HCCC are generally greater, indicating that increasing HCC-related cellular secretions and lipid droplets cause image eigenvalue changes, such as an increase in entropy and contrast, and a decrease in energy. The HCC-related changes in the cell nucleus and nuclear membrane trigger a slight energy reduction according to the experimental results. One can see that the entire eigenvalue distribution accurately reflects the HCCC morphological changes, which is helpful for determining early HCCC damage degrees and performing classification.

The PCLT and HCCT specimens were investigated using the SR-FTIR technique to analyze HCC-related biological macromolecular vibration absorptions, which is helpful for the discrimination of small changes in IR spectral positions and intensities. In Table 3, one can see

Fig. 9 (Color online) Calculated results for morphological eigenvalues based on the GGCM calculation of HCCC and PCLC. **a** Image energy, **b** image entropy, **c** image contrast, and **d** image correlation



that the N–H stretching vibration spectra of HCC shifts to higher wavenumbers more significantly based on the varying lengths of N–H chains. This implies that the HCC cellular chemical environment changes significantly as well. The symmetric and antisymmetric C–H stretching vibration spectra of the HCC samples, which represent the methyl and methylene related to cellular proteins and lipids, shift from a range of 2962–2861 cm^{-1} to 3045–2920 cm^{-1} . This indicates that vigorous tumor cell metabolism plays an important role in angiogenesis, HCC proliferation, and metastasis. The absorption peaks of protein amide I and II for HCCT shift to lower wavenumbers at 1625 and 1485 cm^{-1} , which is associated with secondary protein structural changes. This causes the amide conformation to become loose and disordered. The peaks related to nucleic acids and phosphodiester bonds in HCC samples move to lower wavenumbers at 1151 and 1028 cm^{-1} as a result of the breakage of hydrogen bonds and double strands of DNA. The relative absorption intensities of some characteristic IR spectra, including cholesterol (1467 cm^{-1}), RNA (1121 cm^{-1}), glycogen (1045 cm^{-1}), and DNA (1020 cm^{-1}), were selected to compare the differences between 20 control groups and HCC groups based on unpaired *t* test analysis, as shown in Table 1. The peak height ratio of P_{1045}/P_{1467} for HCCT is

greater than that for PCLT based on a greater increase in glycogen content compared to cholesterol content. The P_{1121}/P_{1020} ratio for HCCT is significantly greater than that for PCLT, because it increases with the degree of malignancy of the tumor. The P_{1121}/P_{1020} (RNA/DNA) ratio in HCC groups is also much greater than that in PCLT, which indicates that the ratio of P_{1121}/P_{1020} significantly increases with the malignancy of the tumor and can be considered as a biomarker for determining the degree of tumor differentiation. The peak area ratio $A_{\text{amide I}}/A_{\text{amide II}}$ of HCCT was lower than that of PCLT, indicating that the HCC-induced secondary structures of nuclear proteins differ from those of intermediates, which could be used as a potential criterion for identifying malignant tumors. The peak area ratio $A_{(\text{CH}_3)}/A_{(\text{CH}_2)}$ increases overall, indicating that the chemical conformation of lipid macromolecules changes, including additional branches of the hydrocarbon chain associated with HCC cell division and proliferation.

5 Conclusion

Synchrotron-based PPCT, STXM, and FTIR methods were combined to study HCC microenvironmental manifestations and micro-pathology through trans-scale and

Table 3 Analysis of spectral features based on SR-FTIR

| Peak positions (cm ⁻¹) | | Frequency shift (cm ⁻¹) | Assignment of vibration mode |
|------------------------------------|------|-------------------------------------|---|
| PCLT | HCCT | δ | |
| 3265 | 3364 | 99 | N–H stretching vibrations in protein amide A band |
| 3080 | 3140 | 60 | N–H stretching vibrations in protein amide B band |
| 2861 | 2920 | 59 | CH ₂ symmetric stretching vibrations: lipids and protein side chains |
| 2922 | 2995 | 73 | CH ₂ antisymmetric stretching vibrations: mainly lipids with little protein |
| 2872 | 2931 | 59 | CH ₃ symmetric stretching vibration: mainly proteins with little lipids |
| 2962 | 3045 | 83 | CH ₃ antisymmetric stretching vibration: mainly membrane lipids and intracellular proteins |
| 1745 | 1764 | 19 | C=O stretching vibrations |
| 1649 | 1625 | 24 | Protein Amide I |
| 1534 | 1485 | 49 | Protein Amide II |
| 1453 | 1385 | 68 | CH deformation vibration of cholesterols |
| 1397 | 1305 | 92 | CH ₃ symmetric stretching vibration: mainly proteins with acids |
| 1209 | 1151 | 58 | Symmetric stretching vibrations of nucleic acids and phospholipids |
| 1074 | 1028 | 46 | Antisymmetric stretching vibrations of nucleic acids and phospholipids |
| 985 | 966 | 19 | Stretching vibrations of deoxyribose and phospholipids |

| Relative absorption intensity | | | |
|--|--------|--------|----------------|
| Ratios of vibrational absorption | PCLT | HCCT | <i>p</i> value |
| P_{1045}/P_{1467} | 1.589 | 1.894 | ** |
| P_{1121}/P_{1020} | 2.796 | 3.014 | ** |
| $A_{\text{amide I}}/A_{\text{amide II}}$ | 2.6323 | 1.921 | * |
| $A_{(\text{CH}_3)}/A_{(\text{CH}_2)}$ | 0.3921 | 0.6943 | * |

**Denotes < 0.01, *denotes < 0.05

multi-modality visualization, correlation analysis, and auto-diagnosis based on BP-NN machine learning. The PPCT and STXM techniques provided insights into the micro-morphological and cellular structural changes in HCCT for clinical diagnosis, revealing that macro-tumor development depends on the tissue inflammatory microenvironment and tumor-derived exosomes. The formation of microcystic clusters gradually develops into sinusoid microvascular infiltration through the abnormal multiplication of tumor cells, eventually leading to the formation of a tumor angiogenesis network. The cytomorphological feature changes stemming from abnormal HCC cell metabolism result in a common inflammatory response in tumor boundary regions. FTIR micro-spectroscopy effectively measured the HCC-related feature spectra, shifting, and chemical distributions of cellular lipids, proteins, and nucleic acid changes, which explained the abnormal metabolism and proliferation of HCC cells at the level of biomolecular mechanisms. Therefore, the proposed synchrotron-based multi-modality method can provide a quantitative, trans-scale comprehensive analysis technique for biomedical specimens, which could enable

the auto-classification and diagnosis of early stage tumor microenvironments based on BP-NN machine learning.

Acknowledgements We thank the staff from the BL13HB beamline of the X-ray Imaging and Biomedical Center, BL08U1-A beamline of the Soft X-ray Spectro-Microscopy Center, BL06B beamline of the Dynamic Beamline: IR Branch at the Shanghai Synchrotron Radiation Facility, and BL01B beamline of the National Facility for Protein Science in Shanghai for their assistance with data collection.

Author contributions All authors contributed to the study conception and design. Material preparation, data collection and analysis were performed by Gong-Xiang Wei, Sui-Xia Zhang, Fu-Li Wang, Zhao Li, Yan-Ling Xue, and Te Ji. The first draft of the manuscript was written by Gong-Xiang Wei and Hui-Qiang Liu and all authors commented on previous versions of the manuscript. All authors read and approved the final manuscript.

References

1. H. Liu, X. Ji, Y. Ma et al., Quantitative characterization and diagnosis via hard X-ray phase-contrast microtomography. *Micro. Res. Tech.* **81**, 1173 (2018). <https://doi.org/10.1002/jemt.23114>
2. P. Wang, Z. Chen, D. Xing et al., Multi-parameter characterization of atherosclerotic plaques based on optical coherence

- tomography, photoacoustic and viscoelasticity imaging. *Opt. Express* **28**, 13761 (2020). <https://doi.org/10.1364/OE.390874>
3. X. Ji, H. Liu, Y. Xing et al., Quantitative evaluation on 3D fetus morphology via X-ray grating based imaging technique. *Int. J. Imaging Syst. Technol.* **29**, 677 (2019). <https://doi.org/10.1002/ima.22354>
 4. H. Tan, D. Wang, R. Li et al., A robust method for high-precision quantification of the complex three-dimensional vasculatures acquired by X-ray microtomography. *J. Synchrotron Radiat.* **23**, 1216 (2016). <https://doi.org/10.1107/S1600577516011498>
 5. Y. Zhao, S. Yang, Y. Wang et al., In vivo blood viscosity characterization based on frequency-resolved photoacoustic measurement. *Appl. Phys. Lett.* **113**, 143703 (2018). <https://doi.org/10.1063/1.5039538>
 6. C. Kamezawa, T. Numano, Y. Kawabata et al., X-ray elastography by visualizing propagating shear waves. *Appl. Phys. Express* (2020). <https://doi.org/10.35848/1882-0786/ab7e06>
 7. S. Yao, J. Fan, Z. Chen et al., Three-dimensional ultrastructural imaging reveals the nanoscale architecture of mammalian cells. *IUCrJ* **5**, 141–149 (2018). <https://doi.org/10.1107/S2052252517017912>
 8. J.Z. Hu, T.D. Wu, Z. Lei et al., Visualization of microvasculature by x-ray in-line phase contrast imaging in rat spinal cord. *Phys. Med. Biol.* **57**, N55 (2012). <https://doi.org/10.1088/0031-9155/57/5/N55>
 9. F. Wang, P. Zhou, K. Li et al., Sensitive imaging of intact microvessels in vivo with synchrotron radiation. *IUCrJ* **7**, 793 (2020). <https://doi.org/10.1107/S2052252520008234>
 10. G. Wei, Y. Liu, X. Ji et al., Micro-morphological feature visualization auto-classification. *Cancer Med.* **10**, 2317 (2020). <https://doi.org/10.1002/cam4.3796>
 11. J. Xiu, Y. Liu, B. Wang et al., Quantitative toxicological study of dose-dependent arsenic-induced cells via synchrotron-based STXM and FTIR measurement. *Analyst* **145**, 4560 (2021). <https://doi.org/10.1039/d0an00346h>
 12. Q. Yang, B. Deng, G. Du et al., X-ray fluorescence computed tomography with absorption correction for biomedical samples. *X-Ray Spectrom.* **43**, 278 (2014). <https://doi.org/10.1002/xrs.2550>
 13. N.S. Farrag, A.M. Amin, Preliminary evaluation of the radiotherapeutic efficacy of ¹³¹I-atrovastatin in rats with hepatocellular carcinoma. *Nucl. Sci. Tech.* **31**(11), 106 (2020). <https://doi.org/10.1007/s41365-020-00819-1>
 14. Y. Yin, K. Luo, Z. Xie et al., An incompatibility problem and solution of multimodal image-guided radiotherapy based on domestic equipment. *Nucl. Tech.* **44**, 030301 (2021). <https://doi.org/10.11889/j.0253-3219.2021.hjs.44.030301> (in Chinese)
 15. Y. Zhou, X. Gao, C. Liu et al., The elements and specification of ¹⁸F-FDG PET-CT and PET-MR tumor imaging report in Shanghai. *Nucl. Tech.* **44**, 010001 (2021). <https://doi.org/10.11889/j.0253-3219.2021.hjs.44.010001> (in Chinese)
 16. Y. Yang, N. Li, Bioinformatic analysis of differentially expressed genes in tumor-associated fibroblasts after ionizing radiation. *J. Radiat. Res. Radiat. Process.* **38**(1), 32–41 (2020). <https://doi.org/10.11889/j.1000-3436.2020.rj.38.010302> (in Chinese)
 17. B. Li, K. Hu, X. Li, Automated radiosynthesis and preliminary Micro-PET/CT imaging of [¹⁸F] AIF-NOTA-P-L-Lys⁶-GnRH. *Nucl. Tech.* **42**, 080303 (2019). <https://doi.org/10.11889/j.0253-3219.2019.hjs.42.080303> (in Chinese)
 18. J. Chen, Y. Fu, D.S. Day et al., VEGF amplifies transcription through ETS1 acetylation to enable angiogenesis. *Nat. Commun.* **8**, 1 (2018). <https://doi.org/10.1038/s41467-017-00405-x>
 19. Y. Fu, H. Peng, X. Zhang et al., Assessment of fibrotic tissue and microvascular architecture by in-line phase-contrast imaging in a mouse model of liver fibrosis. *Eur. Radiol.* **26**, 2947 (2016). <https://doi.org/10.1007/s00330-015-4173-6>
 20. J.H. Duan, C.H. Hu, H. Chen et al., High-resolution micro-CT for morphological and quantitative assessment of the sinusoid in human cavernous hemangioma of the liver. *PLoS ONE* **8**, e53507 (2013). <https://doi.org/10.1371/journal.pone.0053507>
 21. Y. Cao, Y. Zhang, X. Yin et al., 3D visualization of the lumbar facet joint after degeneration using propagation phase contrast micro-tomography. *Sci. Rep.* **6**, 1 (2016). <https://doi.org/10.1038/srep21838>
 22. H. Liu, X. Ji, L. Sun et al., Visualization and pathological characteristics of hepatic alveolar echinococcosis with synchrotron-based X-ray phase sensitive micro-tomography. *Sci. Rep.* **6**, 1 (2016). <https://doi.org/10.1038/srep38085>
 23. J. Hu, T. Wu, L. Zeng et al., Visualization of microvasculature by X-ray in-line phase contrast imaging in rat spinal cord. *Phys. Med. Biol.* **57**, N55 (2012). <https://doi.org/10.1088/0031-9155/57/5/N55>
 24. P. Coan, A. Bravin, G. Tromba et al., Phase-contrast X-ray imaging of the breast: recent developments towards clinics. *J. Phys. D Appl. Phys.* **46**, 494007 (2013). <https://doi.org/10.1088/0022-3727/46/49/494007>
 25. A. Bravin, J. Keyrilainen, M. Fernandez et al., High-resolution CT by diffraction-enhanced x-ray imaging: mapping of breast tissue samples and comparison with their histo-pathology. *Phys. Med. Biol.* **52**, 2197 (2007). <https://doi.org/10.1088/0031-9155/52/8/011>
 26. H.Q. Liu, C.S. Zhang, X.X. Fan et al., Robust phase-retrieval-based X-ray tomography for morphological assessment of early hepatic echinococcosis infection in rats. *PLoS ONE* **12**, e0183396 (2017). <https://doi.org/10.1371/journal.pone.0183396>
 27. B. Chen, G. Feng, B. He et al., Silole-based red fluorescent organic dots for bright two-photon fluorescence in vitro cell and in vivo blood vessel imaging. *Small* **12**, 782 (2016). <https://doi.org/10.1002/smll.201502822>
 28. C.P. Wang, Z.J. Xu, H.G. Liu et al., Soft X-ray ptychography method at SSRF. *Nucl. Sci. Technol.* **28**, 74 (2017). <https://doi.org/10.1007/s41365-017-0227-6>
 29. T. Ji, Y. Tong, H. Zhu et al., The status of the first infrared beamline at Shanghai synchrotron radiation facility. *Nucl. Instrum. Methods. A* **788**, 116 (2015). <https://doi.org/10.1016/j.nima.2015.03.080>
 30. P. Jovana, V. Danijela, R. Tatjana et al., Gray-level co-occurrence matrix analysis of chromatin architecture in periportal and perivenous hepatocytes. *Histochem. Cell Biol.* **151**, 75 (2019). <https://doi.org/10.1007/s00418-018-1714-5>
 31. H.Q. Liu, T.Q. Xiao, H.L. Xie et al., Nondestructive material characterization of meteorites with synchrotron-based high energy x-ray phase micro-computed tomography. *J. Phys. D Appl. Phys.* **50**, 055301 (2017). <https://doi.org/10.1088/1361-6463/aa4f31>
 32. C.P. Wang, Z.J. Xu, H.G. Liu et al., Background noise removal in x-ray ptychography. *Appl. Optics* **56**, 2099 (2017). <https://doi.org/10.1364/AO.56.002099>
 33. P.D. Kumar, Feature extraction and selection of kidney ultrasound images using GLCM and PCA. *Procedia Comput. Sci.* **167**, 1722 (2020). <https://doi.org/10.1016/j.procs.2020.03.382>
 34. T. Vujasinovic, J. Pribic, K. Kanjer et al., Gray-level co-occurrence matrix texture analysis of breast tumor images in prognosis of distant metastasis risk. *Microsc. Microanal.* **21**, 646 (2015). <https://doi.org/10.1017/S1431927615000379>
 35. S. Kaminskyj, K. Jilkine, A. Szeghalmi et al., High spatial resolution analysis of fungal cell biochemistry—bridging the analytical gap using synchrotron FTIR spectromicroscopy. *FEMS Microbiol. Lett.* **284**, 1 (2008). <https://doi.org/10.1111/j.1574-6968.2008.01162.x>
 36. H.Q. Liu, F. Lin, J. Lin et al., Phase-retrieval-based synchrotron X-ray micro-tomography for 3D structural characterization and

- quantitative analysis of agalloch eaglewood. *Wood Sci. Technol.* **52**, 839 (2018). <https://doi.org/10.1007/s00226-018-1004-3>
37. M. Fernandez, J. Keyrilainen, R. Serimaa et al., Human breast cancer in vitro: matching histo-pathology with small-angle x-ray scattering and diffraction enhanced x-ray imaging. *Phys. Med. Biol.* **50**, 2991 (2015). <https://doi.org/10.1088/0031-9155/50/13/002>
38. H.G. Liu, Z.J. Xu, C.P. Wang et al., Soft X-ray spectro-ptychography for air pollution particulates. *Microsc. Microanal.* **24**, 44 (2018). <https://doi.org/10.1017/S1431927618012655>
39. H.G. Liu, J.F. Cao, Y. Wang et al., Soft x-ray spectroscopic end-station at beamline 08U1A of Shanghai Synchrotron Radiation Facility. *Rev. Sci. Instrum.* **90**, 043103 (2019). <https://doi.org/10.1063/1.5080760>
40. Z. Liu, Y. Tang, F. Chen et al., Synchrotron FTIR micro-spectroscopy reveals early adipo-genic differentiation of human mesenchymal stem cells at single-cell level. *Biochem. Biophys. Res. Commun.* **478**, 1286 (2016). <https://doi.org/10.1016/j.bbrc.2016.08.112>
41. S. Lang, P. Schachtschneider, C. Moser et al., Dual targeting of Raf and VEGF receptor 2 reduces growth and metastasis of pancreatic cancer through direct effects on tumor cells, endothelial cells, and pericytes. *Mol. Cancer Ther.* **7**, 3509 (2008). <https://doi.org/10.1158/1535-7163.mct-08-0373>
42. J. Tan, P. Pickhardt, Y. Gao et al., 3D-GLCM CNN: a 3-dimensional gray-level co-occurrence matrix-based CNN model for polyp classification via CT colonography. *IEEE T. Med. Imaging.* **39**, 2013 (2019). <https://doi.org/10.1109/TMI.2019.2963177>
43. G.S. Hong, J.C. Lee, J.T. Robinson et al., Multifunctional in vivo vascular imaging using near-infrared II fluorescence. *Nat. Med.* **18**, 1841 (2012). <https://doi.org/10.1038/nm.2995>

Publisher's Note Springer Nature remains neutral with regard to jurisdictional claims in published maps and institutional affiliations.